

# Simulating Brain Tumor Heterogeneity with a Multiscale Agent-Based Model:

## Linking Cell Signaling, Motility Bias & Expansion Rate

Le Zhang, Costas G. Strouthos<sup>#</sup>, Zhihui Wang, and Thomas S. Deisboeck<sup>\*</sup>

Complex Biosystems Modeling Laboratory, Harvard-MIT (HST) Athinoula A. Martinos Center for Biomedical Imaging, Massachusetts General Hospital, Charlestown, MA 02129, USA.

**Running Title:** Simulating Tumor Heterogeneity with a Multiscale Agent-Based Model  
**Keywords:** glioma, epidermal growth factor receptor, cancer heterogeneity, agent-based model.  
**Abbreviations:** *ECM* = extracellular matrix; *EGF(R)* = epidermal growth factor (receptor); *ICP* = intracranial pressure; *MAPK* = mitogen activated protein kinase; *MMP* = matrix metalloproteinase; *PLC $\gamma$*  = phospholipase C $\gamma$ ; *TGF $\alpha$*  = transforming growth factor  $\alpha$ .

### \*Corresponding Author:

Thomas S. Deisboeck, M.D.  
Complex Biosystems Modeling Laboratory  
Harvard-MIT (HST) Athinoula A. Martinos Center for Biomedical Imaging  
Massachusetts General Hospital-East, 2301  
Bldg. 149, 13th Street  
Charlestown, MA 02129  
Tel: 617-724-1845  
Fax: 617-726-7422  
Email: [deisboec@helix.mgh.harvard.edu](mailto:deisboec@helix.mgh.harvard.edu)

<sup>#</sup> Current address: École Polytechnique Fédérale de Lausanne (EPFL), BCH 3121, CH-1015 Lausanne. Email: [costas.strouthos@epfl.ch](mailto:costas.strouthos@epfl.ch)

## ABSTRACT

We have extended our previously developed 3D multi-scale agent-based brain tumor model to simulate tumor heterogeneity and to analyze its impact across the scales of interest. While our algorithm continues to employ an epidermal growth factor receptor (EGFR) gene-protein interaction network to determine the cells' phenotype, it now adds an explicit treatment of biomechanical pressure to the model's biochemical microenvironment. We simulate a simplified tumor progression pathway that leads to the emergence of five distinct glioma cell clones with different EGFR density and cell adhesion patterns. The *in silico* results show that microscopic tumor heterogeneity can impact the tumor system's multicellular growth patterns. Our findings further confirm that EGFR density plays an important role in processing the chemotactic motility bias that results in increased persistence of the more aggressive clonal populations which also switch earlier from proliferation-dominated to a more migratory phenotype. However, while the EGFR density within each clone remains rather stable, it is the fluctuations in active phospholipase C $\gamma$  (*PLC $\gamma$* ) that impact the clone's expansion rate changes the most. Intriguingly, in aggressive clones that exhibit a high EGFR density, the downstream signaling cascade appears to process signals more efficiently as indicated in a more sensitive *PLC $\gamma$*  -'switch'. Potential implications from this *in silico* work for experimental and computational studies are discussed.

## 1. INTRODUCTION

We present the extension of our previously developed three-dimensional (3D) *agent-based*, multi-scale brain tumor model to incorporate a simplified glioma *progression pathway* in an effort to study the impact of clonal heterogeneity on tumor growth dynamics. For the micro-macroscopic environment, we expanded the initial setup (Athale, et al., 2005, 2006; Zhang et al., 2007) by introducing an element of *intracranial pressure* or ICP (Hakim et al., 1971; Nagashima et al., 1987). Consequently, the gradients of chemoattractants such as glucose, oxygen tension and transforming growth factor alpha (TGF $\alpha$ ) arise not only from the competition between diffusion (Sander & Deisboeck, 2002; Throne et al., 2004; Carmeliet & Jain, 2000) and convection (Jain, 1987) due to the cells' consumption or secretion, but cells can now also locally remodel their microscopic environment as ICP correlates with tumor growth dynamics (Sklar & Elashvili, 1977; Marmarou et al., 1975) and impacts the cells' migration rate (Chicoine & Silbergeld, 1995). Specifically, we modeled the chemotactically attracted cells as follows: once the concentration of the so called homotype attractant (Habib et al., 2003), in this case TGF $\alpha$ , substantially exceeds that of the heterotype attractant (Castro et al., 2005) such as glucose or oxygen, the homotype attractant plays a much more important role for directing cell attraction and vice versa. For the molecular environment, each cell is equipped with an epidermal growth factor receptor (EGFR) *gene-protein interaction pathway* (Athale et al., 2005, 2006; Zhang et al., 2007) that is implicitly integrated with a simplified *cell cycle* module (Alarcon et al., 2004). The pathway molecule 'activated phospholipase C $\gamma$ ' (PLC $\gamma$ ) is critical in determining the cell phenotype which represents experimental results reported by Dittmar et al. (2002). However, other than in our previous works where heterogeneity arose only from phenotypic alterations of an otherwise mono-clonal tumor, here, we have integrated a simplified cancer progression model (based on Sole & Deisboeck (2004)) to generate a heterogeneous brain tumor that eventually consists of five distinct clonal

populations that emerged through mutational events. These clones differ in their EGFR density in addition to being able to adjust their phenotypic behavior readily to the micro-environmental conditions. The sub-clones with higher EGF receptor density are more aggressive (Steinbach et al., 2004), exhibit less tumor cell-tumor cell adhesion (Jones et al., 2001; Natarajan, et al., 2003; Riemenschneider, et al., 2005) and operate with an inefficient metabolism (Boussouar & Benahmed, 1999; Smith, 2004); yet, they achieve a higher chemotactic search precision to move faster along the environment's least resistance, most permission and highest attraction paths (Deisboeck et al., 2001). We will discuss the results and their potential implications, and introduce future work.

## 2. PREVIOUS WORKS

Earlier tumor models focused primarily *either* on the micro-macroscopic *or* on the molecular level to simulate tumor growth and migration. For instance, for the micro-macroscopic scale, Mansury et al. (2002) and Mansury & Deisboeck (2003, 2004a) proposed a two-dimensional (2D) agent-based model in which the spatio-temporal expansion of malignant brain tumor cells is guided by environmental heterogeneities (mechanical confinement, toxic metabolites and nutrient sources) in order to gain more insight into the systemic effect of such cellular chemotactic search precision modulations. For the molecular scale, Schoeberl et al. (2002) built up a computational model to describe the dynamics of the MAPK cascade activated by EGF receptors and Araujo et al. (2005) developed an EGFR signaling network model that not only shows the protein dynamics in the EGFR pathway but also predicts the therapeutic effect of inhibitors on the molecular network. In an effort to develop a cell cycle module, Alarcon et al. (2004) extended the work of Tyson & Novak (2001) to model the cancer cell cycle process under hypoxic conditions. Additionally, to simulate mutation among different clones, Sole &

Deisboeck (2004) revised the previous quasispecies model of Swetina & Schuster (1982) to research the impact of genetic instability on tumor growth. While these models undoubtedly are useful at their particular scale, the quest of studying the tumor as a biological system that crosses scales requires a *multiscale* modeling approach. Therefore, in Mansury & Deisboeck (2004b) and Athale et al. (2005, 2006) our group developed a 2D multi-scale agent-based tumor models to integrate both, the molecular and micro-macroscopic environments. Specifically, in Athale et al. (2005) we put forward an EGFR gene-protein interaction pathway in which activated *PLC $\gamma$*  is employed to determine the cell phenotype. Subsequently, in Athale et al. (2006) we then compared the biological behaviors of glioma cell clones with varied EGFR density. Building on this work, in Zhang et al. (2007) we recently introduced a 3D multi-scale agent-based brain tumor model which explicitly includes a cell cycle description. However, this multi-scale model has a number of shortcomings that include simulating a monoclonal, and thus unrealistically genetically stable tumor, and it also suffers from a rather simplistic description of the tissue microenvironment. In an effort to model these features more realistically the subsequent section will describe the setup of a much more sophisticated 3D multi-scale brain tumor model that includes a biphasic brain tissue (Sklar & Elashvili, 1977) and incorporates the emergence of heterogonous tumor cell clones.

### 3. MATHEMATICAL MODEL

As before, this multi-scale agent-based brain tumor model includes macro-microscopic and molecular environments that interact with each other. The following sections describe these environments and their relationships in detail.

#### 3.1. Macro-microscopic environment

### 3.1.1. Clonal heterogeneity

Here, a slice of virtual brain tissue is modeled with a  $100*100*100$  3D rectangular lattice as depicted in **Figure 1**. A continually replenished nutrient source, representing a blood vessel, is located in Cube 4.

#### Figure 1

To yield tumor heterogeneity, an element of genetic instability is introduced that is based on the mutation model presented by Sole & Deisboeck (2004). Our “progression pathway” here incorporates five glioma cell clones (A, B, C, D and E) that emerge sequentially, and that are distinct in their EGFR receptor density (**Figure 2**). Based on experimental data, in our setup, cell clones with higher EGFR receptor density are more aggressive (Westermarck et al., 1982; Lund-Johansen et al., 1990; Steinbach et al., 2004) and exhibit less tumor cell-tumor cell adhesion (Jones et al., 2001; Natarajan, et al., 2003; Riemenschneider, et al., 2005; Christofori, 2006).

#### Figure 2

In the beginning, five hundred clone A cells are initialized in the center of the lattice. As a first iteration, the model implements a *linear* progression pathway in assuming that clone A can only mutate to B, clone B to C, C to D, and D to E. The respective mutation rates depend on the cell’s proliferation period and are listed in **Table 1**.

#### Table 1

To mimic progression from a relatively genetically stable precursor, we set the mutation rate from clone A to B as  $1 - \frac{\text{B Proliferation Period}}{\text{A Proliferation Period}} = 12.5\%$ . Applying the same calculation for the remaining clones, we deduce a mutation rate from B to C of 14.2%, from C to D of 16.7% and D to E of 20%.

### 3.1.2. Chemoattractants

Transforming growth factor alpha (TGF $\alpha$ ) is a protein that not only can affect the secreting tumor cell itself, hence generates an ‘‘autocrine’’ feedback loop, but also can impact bystander cells, an effect known as ‘‘paracrine’’. Habib et al. (2003) refers to this soluble chemical effector, as *homotype* chemoattractant. Conversely, glucose and oxygen, not produced by tumor cells, are denoted as *heterotype* attractants (Castro et al., 2005). Our setup places a blood vessel in Cube 4 (at  $x$ - $y$ - $z$  coordinates 85, 85, 85) to supply glucose, TGF $\alpha$  and oxygen for the developing brain tumor. Initially, these chemoattractants are dispersed by normal distribution described in **Eq. 1-3**:

$$X_1^{ijk} = T_m \exp(-2d_{ijk}^2 / \sigma_t^2) \quad (1)$$

$$X_{14}^{ijk} = G_a + (G_m - G_a) \exp(-2d_{ijk}^2 / \sigma_g^2) \quad (2)$$

$$k_{44}^{ijk} = k_a + (k_m - k_a) \exp(-2d_{ijk}^2 / \sigma_o^2) \quad (3)$$

In **Eq. 1**,  $T_m$  stands for the maximum TGF $\alpha$  ( $X_1$ ) concentration in the tumor (Moskal et al., 1995),  $\sigma_t$  is the parameter that controls the dispersion of the TGF $\alpha$  level. In **Eq. 2**,  $G_a$  is the minimum blood glucose ( $X_{14}$ ) level while  $G_m$  stands for the maximum concentration of glucose in blood (Freyer and Sutherland, 1986), with  $\sigma_g$  being the parameter controlling the dispersion of glucose. Likewise, in **Eq. 3**,  $k_a$  is the minimum oxygen tension and  $k_m$  represents the maximum oxygen tension ( $k_{44}$ ) (Alarcon et al., 2004; Zhang et al., 2007),  $\sigma_o$

is the parameter controlling the dispersion of the oxygen tension level, and  $d_{ijk}$  is the L-infinity (Mansury et al., 2002) distance to the center of Cube 4. During the simulation, the cell will take up glucose to maintain its metabolism and secrete TGF $\alpha$  (Athale et al., 2005) triggering both paracrine and autocrine biological behavior that is described by **Eq. 4-5**:

$$X_1^t = X_1^{t-1} + S_t \quad (4)$$

$$X_{14}^t = X_{14}^{t-1} - r_n, n = A, B, C, D, E \quad (5)$$

In **Eq. 4-5**,  $t$  represents the time step,  $S_t$  is the TGF $\alpha$  secretion rate (Forsten and Lauffenburger, 1992) and  $r_n$  is the cell's glucose uptake coefficient (Shrivastava et al., 2006) for each clone. Because Smith (2004) argues that the metabolism of cancer cells is approximately eight times larger than the metabolism of normal cells and since Shrivastava et al. (2006) discovered that for U87 human glioma cells the glucose uptake rate is 0.77 pmol/h per cell, we assign each clone (A, B, C, D and E) a different glucose uptake rate related to its EGFR density, which is listed in the **Table 2**.

**Table 2**

### 3.1.3. Biomechanics

Introducing intracranial pressure (ICP) to our model, we first refer to Pena et al. (1999) who considered brain tissue being a biphasic material encompassing both solid tissue and interstitial fluid (Hakim et al., 1971; Nagashima, et al., 1987). Greenberg's (2001) report that normal intracranial pressure ranges from 10-15mm Hg, with life threatening values of around 25-30mm Hg, led us to set the ICP between 10-30mm Hg, initially normally distributed as described by **Eq. 6**,

$$P^{ijk} = P_b + (P_u - P_b) \exp(-2d_{ijk}^2 / \sigma_p^2) \quad (6)$$

where  $P^{ijk}$  stands for the ICP of tissue cube 2, 3 and 4, with  $P_b$  and  $P_u$  being the minimum and maximum intracranial pressure, respectively. Because of the difference of pressure and gradient, the aforementioned chemoattractants such as glucose,  $TGF_\alpha$  and oxygen, simultaneously keep *diffusing* (Athale et al., 2005, 2006; Zhang et al., 2007) and *convecting* (Jain, 1987) during the simulation by **Eq.7-9**.

$$\frac{\partial X_1^{ijk}}{\partial t} = D_2 \nabla^2 X_1^{ijk} + K \nabla P^{ijk} \nabla X_1^{ijk}, t = 1, 2, 3 \dots \quad (7)$$

$$\frac{\partial X_{14}^{ijk}}{\partial t} = D_1 \nabla^2 X_{14}^{ijk} + K \nabla P^{ijk} \nabla X_{14}^{ijk}, t = 1, 2, 3 \dots \quad (8)$$

$$\frac{\partial k_{44}^{ijk}}{\partial t} = D_o \nabla^2 k_{44}^{ijk} + K \nabla P^{ijk} \nabla k_{44}^{ijk}, t = 1, 2, 3 \dots \quad (9)$$

where  $D_1$  is the diffusion coefficient of glucose (Sander and Deisboeck, 2002),  $D_2$  is the  $TGF_\alpha$  diffusion coefficient (Thorne et al., 2004) and  $D_o$  stands for the diffusion coefficient of oxygen (Carmeliet and Jain, 2000);  $K$  represents the hydraulic permeability (Pena et al., 1999). Furthermore, Chicoine et al. (1995) reported an average glioma cell velocity of  $4.8 \mu\text{m/h}$  *in vivo* and of  $12.5 \mu\text{m/h}$  *in vitro*. We reflect these experimental data in setting a maximum cell velocity of around  $11 \mu\text{m/h}$  and minimum velocity of around  $3 \mu\text{m/h}$  *in silico* and arrive at **Eq. 10** which links ICP with the cells' migration rate as follows,

$$v = \omega / P^{ijk} \quad (10)$$

where  $v$  is the speed of the moving cell and  $\omega$  is a weight constant listed in **Table 2**. Since ICP is dynamically changing at each lattice site, this cell motility speed varies at different locations and over time. The fact that tumor growth and ICP are related (Marmarou et al., 1975; Gordon et al., 2003) led Sklar & Elashvili (1977) to put forward a 'pressure-volume function' of *brain elasticity* based on their clinical data. Additionally, it is well known that glioma cells exhibit *proteolytic activity* in secreting enzymes or, more specifically, matrix metalloproteinases (MMPs) (Nakano et al., 1995; Choe et al., 2002); Chintala et al. (1999)

then reported that MMPs can degrade almost all known ECM components and seem to play important roles in mediating glioblastoma tumor cell invasion. We have therefore revised the above cited pressure-volume function of brain tissue in an effort to simulate the relationship between ICP, tumor growth and MMPs with **Eq. 11**,

$$dP^{ijk} = \frac{P^{ijk}}{\eta \cdot V_T} \quad (11)$$

where  $\eta$  is a dimensionless constant (Sklar & Elashvili, 1977) listed in **Table 2**. We note that when a migrating cell enters or leaves a lattice site, volume ( $V_T$ ) of **Eq. 11** refers to the [total] volume of migrating cells but when a new proliferative cell is created at this the lattice site, volume ( $V_T$ ) represents the proliferative and quiescence cells' volume.

#### 3.1.4. Spatial search process

Representing the biological mechanism of *chemotaxis* we have again implemented a search mechanism as put forward already in Mansury et al. (2002; 2003).

$$T_{ijk} = \psi_n \cdot L_{ijk} + (1 - \psi_n) \varepsilon_{ijk}, n = A, B, C, D, E \quad (12)$$

where  $T_{ijk}$  stands for the perceived attractiveness of location  $(i, j, k)$ ,  $L_{ijk}$  represents the correct, non-erroneous evaluation of location  $(i, j, k)$  where  $\varepsilon_j \sim N(\mu, \sigma^2)$  is an error term that is normally distributed with mean  $\mu$  and variance  $\sigma^2$ . The parameter  $\psi_n$  is positive between zero and one,  $0 \leq \psi_n \leq 1$ , and represents the extent of the *search precision* (with '0' exhibiting purely *random walk* behavior, and '1' being fully *biased* without any error in signal processing), and the subscribe of  $\psi$  represents the different clones.

The definition of the Von Neumann and Moore neighborhoods usually are restricted to 2D lattices. We therefore define 3D Von Neumann neighborhood and 3D Moore neighborhood as detailed in **Eq.13-14**:

$$N_{(x_0, y_0, z_0)}^v = \{(x, y, z) : |x - x_0| + |y - y_0| + |z - z_0| \leq 1\} \quad (13)$$

$$N_{(x_0, y_0, z_0)}^m = \left\{ \begin{array}{l} \{(x, y, z) : |x - x_0| + |y - y_0| \leq 1\} \\ \{ \{(x, y, z) : |x - x_0| + |z - z_0| \leq 1\} \\ \{ \{(x, y, z) : |y - y_0| + |z - z_0| \leq 1\} \} \end{array} \right\} \quad (14)$$

Here,  $(x_0, y_0, z_0)$  is the current location of the cell and  $(x, y, z)$  represents the coordinates of its neighborhood.

It has been well established that cancer cells differ from normal cells in a variety of ways which include uncontrolled proliferation, loss of contact inhibition, progressive lack of tumor cell-tumor cell adhesion and invasion (Runowicz et al, 2005; Hanahan & Weinberg, 2000). Also, Athale et al. (2006) already demonstrated in separate simulation runs that *in silico*, glioma cells with higher EGFR density are more aggressive with faster migration and lower proliferation rate. We therefore incorporate in our expanded model here not only that the search precision of clones C, D, E is higher than that of clones A and B, but also clone C, D and E's spatial "permission" is larger, reflecting its progressive loss of tumor cell-tumor cell adhesion. These relationships are detailed in **Table 3**.

**Table 3**

As discussed earlier,  $L_{ijk}$  is the correct, non-erroneous evaluation of location, which includes the impact of mechanical resistance, homotype and heterotype chemoattractants. **Eq. 15** models this biological behavior, i.e., if a cell stays in the location  $(x_0, y_0, z_0)$  and the sum of its 3D Von Neumann neighborhood  $\text{TGF}\alpha \left( \sum_{N_{(x_0, y_0, z_0)}^v} X_1 \right)$  is greater than glucose concentration

( $\sum_{N_{(x_0, y_0, z_0)}^v} X_{14}$ ), then this cell is subjective to choose the homotype attractant, otherwise the cell is

attracted by the heterotype cue.

$$L_{ijk} = X_1^{ijk} - \gamma_1 P^{ijk}, \text{ if } \frac{\sum X_1}{X_1} > \frac{\sum X_{14}}{X_{14}} \quad (15a)$$

$$L_{ijk} = X_{14}^{ijk} - \gamma_2 P^{ijk}, \text{ if } \frac{\sum X_1}{X_1} < \frac{\sum X_{14}}{X_{14}} \quad (15b)$$

where  $\gamma_1$  and  $\gamma_2$  are two scales to adjust the difference between chemoattractant and mechanical resistance.

### 3.1.5. Cell phenotype

As before, we simulate four different cellular phenotypes, i.e. migration, proliferation, quiescence and apoptosis – now, however, for each of the five different glioma cell clones. We again implement the concept of ‘dichotomy’ for glioma cells, first put forward by Giese et al. (1996) which argues on the basis of mounting experimental data that migration and proliferation are mutually exclusive behaviors that can happen in sequence, yet hardly at the same time in the same cell. Using breast cancer cells, Dittmar et al. (2002) discovered that *PLC $\gamma$*  is activated transiently, that is, to a greater extent during migration and more gradually during proliferation. Building on this experimental data, Athale et al. (2005, 2006) and Zhang et al. (2007) employ a *PLC $\gamma$*  threshold ( $\sigma_{PLC}$ ) to model this biological *switching behavior* as

$$MP[X_{11}] = \left[ \frac{dX_{11}}{dt} \right] \quad (16)$$

where *MP* is the migration power that equals the change of active *PLC $\gamma$*  over time. Once *MP* is greater than the  $\sigma_{PLC}$ , the cell chooses the migratory phenotype, otherwise it undergoes proliferation. We note that there are three possibilities that the cell enters the reversible quiescent state: (1) the cell is unable to find an empty location to migrate to or proliferate into;

or (2) the migration potential (  $MP$  ) is less than  $\sigma_{PLC}$  and  $ppTGF\alpha - EGFR\_s$  is less than  $\sigma_{EGFR}$ ; or, (3) the glucose concentration around the cell drops to critically low values. If the on-site glucose concentration diminishes even further, the cell enters the apoptotic state (Freyer and Sutherland, 1986).

### 3.2. Molecular environment

The molecular setup is described in detail in Zhang et al. (2007). Here, we only briefly summarize the molecular environment and focus on its modifications. Each cell is equipped with an EGFR gene-protein interaction network depicted by **Figure 3**, composed of 14 molecular species in addition to five molecular species involved in our simplified cell cycle representation. These molecular species interact with each other according to mass balance equations, denoted by the general form:

$$\frac{dX_i}{dt} = \alpha_i X_i - \beta_i X_i \quad (17)$$

where  $X_i$  is the mass of  $i$ th ( $i=1-14$ ) molecules comprising the EGFR network and  $\alpha_i, \beta_i$  ( $i=1-14$ ) are the rate of synthesis and degradation rate of EGFR pathway, respectively. Also,  $X_i$  ( $i=15-19$ ) molecules are the components of the cell cycle and  $\alpha_i, \beta_i$  ( $i=15-19$ ) are the coefficients of the cell cycle module. The values of parameters and constants are listed in Zhang et al. (2007). As an important extension of our previous works, a proliferation process has now been *explicitly* integrated into the model in that more aggressive cell clones are associated with a shorter *cell doubling time*.

**Figure 3**

## 4. RESULTS

Our code is implemented in Java (Sun Microsystems, Inc., USA), combined with in-house developed classes for representing molecules, reactions and multi-receptors as a set of hierarchical objects. Running the simulation 10 times with different random normal distribution,  $\sigma_g$ , of glucose (**Eq. 2**), the algorithm requires a total of 70 hrs 46 min of CPU time on a computer with an IBM Bladecenter machine (dual-processor 32-bit Xeons ranging from 2.8-3.2GHz w/2.5GB RAM) and Gigabit Ethernet. Each node runs Linux with a 2.6 kernel and Sun's J2EE version 1.5.

Employing a multi-level growth model, our analysis spans several scales of interest in starting with the overall, macroscopic behavior followed by the multicellular population patterns before focusing on the distinct impact molecular-level dynamics have on microscopic cell phenotypes.

**Volumetric tumor growth dynamics:** We measure the tumor system's [total] volume by counting the number of lattice sites occupied by a tumor cell regardless of its phenotype, hence lumping together both proliferative- and migratory-driven expansion. **Figure 4** shows the tumor's volumetric increase over time for the 10 simulation runs.

### Figure 4

To achieve a higher resolution of analysis, we divide the macroscopic tumor into three microscopic regions, sectioning the distance between the tumor and the nutrient source such as shown in **Figure 5.(a)**: region 1 is closest to the nutrient source, region 3 is farthest from the nutrient source, with region 2 being located in between.

**Tumor heterogeneity:** In an attempt to quantify clonal heterogeneity Maley et al. (2006) defined the so-called *Shannon Index* as  $H = -\sum_i p_i \ln(p_i)$  where  $p_i$  is the frequency of clone  $i$  within the tumor. **Figure 5.(b)** shows this Shannon Index for region 1, 2, and 3 at each time step. While the indices for all three regions generally increase (i.e., exhibit more clonal heterogeneity) region 1 experiences an unexpected drop around  $t = 100$ , which indicates the emergence of a more homogenous sub-section that is dominated by fewer tumor cell clones.

### Figure 5

Visualizing this type of emergent heterogeneity by orienting us on curve-crossing points seen in **Figure 5.(b)**, we display in **Figure 6.(a)-(c)** representative 3D snapshots of the tumor at time points  $t = 110$ , 225 and 310, noting that one time steps equals 10 hrs. It is evident that the tumor overall expands towards the location of the nutrient source (compare with **Figure 1**).

### Figure 6

**Expansion rate per tumor region:** To support this impression quantitatively, we measure the expansion rate for each sub-region by computing the average expansion radius for each region based on its center. The results show that tumor region 1, i.e., closest to the nutrient source, expectedly expands faster than regions 2 and 3 that are farther from the nutrient source (**Figure 7**). The lesser expansion rate of region 2 versus region 3 is due to the stronger facilitating impact of a lower ICP in region 3 than that of a higher nutrient concentration in region 2.

### Figure 7

**Expansion rate per tumor clone:** The next question to address is then how much of that regional specificity is due to its prevailing clonal population and as such we measure the expansion rate for clone A, B, C, D and E at each time step by computing the average expansion radius for each clone based on the center of each clone. From **Figure 8** one can see that while clone E (with the highest EGFR density per cell) is not the first clone to start migration, it nonetheless exhibits the highest expansion rate. In contrast, although clone A and B with lower EGFR density start to expand much earlier than clone C, D and E, these two lower malignant clones always keep a much smaller expansion rate for most of the simulation.

So far, the results support the notion that a higher density of the more aggressive clone E is responsible for the higher expansion rate in the tumor region that is closest to the nutrient source. This therefore warrants a more detailed look into the phenotypic dynamics of the cancerous clones in general, and of clone E in particular.

### Figure 8

**Phenotypic spectrum per tumor clone:** Turning then to the microscopic analysis level by counting the phenotype fraction of clone A, B, C, D and E at each time step (**Figure 9. (a)-(e)**) it is evident that clones with higher EGFR density are eventually comprised of a larger migratory fraction, while exhibiting a smaller proliferation and quiescence cell population. Specifically, clone E has the largest and most sustained migratory cell population, and, as the curve shows, the “population” crossover between a more stationary, proliferation-dominated to an expansive, migration-dominated clone happens earlier than in the other, less aggressive tumor clones. We also note that, qualitatively, the fluctuations in the curves increase from a

fairly periodic pattern in the lower malignant clones A and B, to a much less regular, noisy pattern in the higher malignant clones.

### Figure 9

**Detrended fluctuation analysis for each tumor clone:** To further describe these fluctuations seen in the phenotype spectra, we employed *Detrended Fluctuation Analysis* (DFA), a technique that has been developed to quantify the correlation property in non-stationary physiological time series (Buldyrev et al., 1993; Hausdorff et al., 1995; Peng et al., 1994, 1995; Ossadnik, et al., 1994). Briefly, the DFA method consists of the following steps. First, it divides each duration of total simulation period,  $T$ , into  $T/d$  non-overlapping windows, each containing  $d$  data points. Next, in each window of size  $d$ , we employ a least-squares curve ( $g_{i,d,t}$ ) fit for the original data then compute the minimum sum-of-squared residuals ( $SSR$ ) for each window as detailed in **Eq. 18**:

$$SSR_{i,d,p} = \sum_{t=p}^{p+d} (g_{i,t} - g_{i,d,t})^2 \quad (18)$$

Finally, we calculate the average  $SSR_{i,d,p}$  over all windows of size  $d$  as described in **Eq. 19**:

$$SSR_{i,d} = \frac{d}{T} \sum_p SSR_{i,d,p} \quad (19)$$

If the time series exhibits the statistical properties of a random walk then DFA would yield  $\sqrt{SSR_{i,d}} \sim d^\alpha$  with  $\alpha = 0.5$ . In contrast, if there is a long range power law autocorrelation, then  $\sqrt{SSR_{i,d}} \sim d^\alpha$  with  $0.5 < \alpha < 1$ . If  $\alpha \geq 1$ , correlations exist yet they cease to be of a power-law form; if  $\alpha \geq 1.5$ , it argues for brown noise. We note that  $\alpha$  is the scaling exponent, i.e., the slope of the curve fit relating  $\log_{10} F(n)$  to  $\log_{10} n$ . Using the DFA tool provided by PhysioNet (<http://www.physionet.org/physiotools/dfa/>), we obtained the results

depicted in **Figure 10**. Applying DFA for the migratory behavior in clone B, C, D and E yields an  $\alpha$  of 1.9978, 1.9509, 1.8887 and 1.6655, respectively. Following the aforementioned definition, this DFA result confirms that cells from these four clones conduct a *biased random walk*<sup>1</sup>.

### Figure 10

**Displacement effectiveness per tumor clone:** While this ‘bias’ should be induced by the chemotactic source located in Cube 4 (compare with **Figure 1**), one needs to still investigate through which mechanism such single cell-based chemotactic search (**Figure 10**) impacts the clones’ distinct overall expansion rate (**Figure 8**). In fact, such signal-directed motility should be reflected in the cells’ ‘persistence’, and so we measure their *displacement effectiveness*<sup>2</sup>. Costa et al. (2005) defined  $D_i$  as the distance between the cell’s initial position and the final position which is described by **Eq. 20**:

$$D_i = \sqrt{(x_i(M-1) - x_i(0))^2 + (y_i(M-1) - y_i(0))^2 + (z_i(M-1) - z_i(0))^2} \quad (20)$$

The total arc length  $L_i$  covered by the cell along that span can be estimated as the sum of the distance between the subsequent position along the trajectory which is depicted by **Eq. 21**:

$$L_i = \sum_{j=1}^{M-1} \sqrt{(x_i(j) - x_i(j-1))^2 + (y_i(j) - y_i(j-1))^2 + (z_i(j) - z_i(j-1))^2} \quad (21)$$

<sup>1</sup> Clone A cannot be analyzed reliably with DFA due to its oscillatory curve.

<sup>2</sup> Since our model simulates both cell migration and proliferation, we used the *proportion* of migratory cells within the [total] tumor cell population to calculate the reported persistence values.

where  $M$  is the final time step of the simulation, and  $x_i$ ,  $y_i$  and  $z_i$  are the coordinates of the cell. The displacement effectiveness  $E_i$  is defined as  $E_i = \frac{D_i}{L_i}$ . It is obvious that  $0 \leq E_i \leq 1$ ; the larger the value of  $E_i$ , the closer  $D_i$  is to  $L_i$ , indicating more effective displacement as shown in **Figure 11**. Despite the standard deviation one can recognize the trend that cells which belong to clones A and B exhibit a lesser displacement effectiveness than C, D and E. This, in turn, indicates more randomness in the spatial behavior of clones A and B, while cell derived from the aggressive clones C, D and particularly E operate with higher spatial persistence in their chemotactically guided movement.

### Figure 11

**Relationship between molecular profile and multicellular behavior per clone:** To summarize these findings we plot the relationship between the key molecular players of the cell signaling network, and the migratory driven tumor expansion. Specifically, **Figure 12** depicts the relationship between the percentage change in EGFR density and active  $PLC_\gamma$  versus the percentage change of a particular cancer cell clone's expansion rate. One can see that **(i)** the percentage change in spatial expansion rate for all clones, low and highly aggressive, depends to a larger degree on the percentage change of active  $PLC_\gamma$  than on a change in EGFR density; and **(ii)** the percentage change of active  $PLC_\gamma$  in clones C, D and E varies within a much smaller range than those for clones A and B.

### Figure 12

## 5. DISCUSSION & CONCLUSIONS

In here, we present an expansion of our 3D multi-scale agent-based brain tumor model that has now been extended to also incorporate an element of genetic instability to simulate glioma progression and to analyze its impact across multiple scales. Building on our previous works (Athale et al., 2005, 2006; Zhang et al., 2007), this model not only encompasses molecular, microscopic and macroscopic scales of observation, but now also integrates both cell doubling time and cell cycle into the cells' proliferation module. Furthermore, heterogeneity exists here both in terms of tumor cell populations as well as with regards to the micro-environmental conditions, most notably in an explicit treatment of intracranial pressure. In the following, we discuss the results in more detail.

The tumor region adjacent to a blood vessel representing nutrient source (i.e., region 1) harbors early on the highest clonal heterogeneity (**Figure 5.(b)**), reflecting the spatio-temporal output of the implemented linear progression path. However, around time step  $t = 100$  this geographic 'tip' region (**Figure 6.(a)-(c)**) becomes increasingly homogeneous due to a *competitive* advantage of the most aggressive clone E with regards to its chemo-sensing ability and high spatial expansion rate. In other words, clone E prevails in its quest to move fastest into the direction of "least resistance, most permission and highest attraction" (Deisboeck et al., 2001), and, in the process, impacting the spatio-temporal patterns of the entire tumor system. However, the micro-environmental conditions closer to the core of the tumor, i.e. for cells in regions 2 and 3 are less selective for clone E and thus continuous tumor progression yields a sustained increase in the Shannon Index that eventually even exceeds the peak value for region 1. One can argue that, other than region 1, regions 2 and 3 allow for an element of temporary *cooperation* between the clones. Since regions 2 and 3 together add up to a larger volume than region 1 alone, this finding corresponds well with another recent

claim of cancer cell cooperation fostering tumorigenesis (Axelrod et al., 2006), and also with the results reported by Maley et al. (2006) on esophagus cancer which indicated that clonal heterogeneity is a greater risk factor for progression to cancer than the expansion of a homogeneous clone with a low Shannon Index value.

The question arises then as to what precisely are the effects of such clonal heterogeneity on tumor growth dynamics? First, due to their higher density of EGF receptors per cell and thus more pronounced chemotactic bias (**Figure 10**) and spatial persistence (**Figure 11**) clones C, D and primarily E exhibit an increased expansion rate (**Figure 8**) that results in the aforementioned faster growth of region 1 (**Figure 7**). Correspondingly, **Figure 9** confirms that these tumor clones with higher EGFR density switch earlier to an invasive phenotype-dominated cell population that operates with a larger fraction of migratory cells, yet with lesser proliferative and quiescent cells. From our *in silico* model emerges that higher EGFR expression leads to faster expansion of tumor areas that harbor more such aggressive cell populations. This, in turn, will result in overall growth asymmetries, i.e., findings that taken together correspond well with reported experimental and clinical results (Westermarck et al., 1982; Lund-Johansen et al., 1990; Steinbach et al., 2004).

Taking advantage of our algorithm's multi-scale design we can relate molecular percolations to the resulting multicellular behavior by summarizing as to how the percentage change of EGFR density and active  $PLC_\gamma$  (i.e. the two most important molecular species in the implemented EGFR signaling pathway) impact the cancer cell clones' spatio-temporal expansion rate. From **Figure 12**, we can tell that (1) regardless of a clone's "clinical" grading, the percentage change in active  $PLC_\gamma$  always has a more substantial impact on the percentage change of the clone's expansion rate than any change in EGFR cell surface density has; and,

equally intriguing, (2) the percentage changes of active  $PLC_\gamma$  of clones C, D and E vary to a lesser degree than those for clones A and B. Taken together, one can deduce that in order to switch to the migratory phenotype cancer cells in clones C, D and E require a lesser percentage change of active  $PLC_\gamma$  than clone A and B. In other words, such aggressive cancer cells are more *sensitive* in processing the EGFR-downstream signaling pathway and more *efficient* in operating the  $PLC_\gamma$  switch. Conversely, although each clone is associated with a different EGFR density, the percentage change of the EGFR concentration for each clone varies only marginally indicating a more *robust* regulation on the EGF-R level. Intriguingly, experimental results already confirm the inhibitory effect a blockage of  $PLC_\gamma$  can have on glioma motility, hence indicating a potential therapeutic strategy (Khoshyomn et al., 1999). This, however, has to be pursued with caution as ongoing collaborative experimental work suggests that knockdown of  $PLC_\gamma$  with siRNA is not only capable of reducing glioma cell migration but, as expected for a ‘switch’, may also lead to a corresponding increase in tumor cell proliferation (Demuth et al., In preparation).

Despite these considerable extensions, our modeling platform of course has still a number of shortcomings that can and should be addressed in future works. For example, we currently rely on a fixed mutation rate between each clone and mutations only occur linearly from A to E, without any non-linear ‘shortcuts’ and without assigning different weight to specific mutations. In subsequent research, we intend to implement a dynamical mutation rate that depends both on intrinsic and extrinsic or microenvironmental factors. Nonetheless, this work significantly enhances our previously introduced platform (Athale, et al., 2005, 2006; Zhang et al., 2007) by including the element of genetic instability, by taking the biomechanical properties of the microenvironment explicitly into account and by integrating both cell cycle and cell doubling time into the cells’ proliferation process. Given the fact that we begin to be

able to validate some of the model's predictions with experimental studies, we firmly believe that this type of interdisciplinary approach holds significant promise to help improve our understanding of cancer progression and its impact on the tumor system's regional and global growth dynamics.

## **ACKNOWLEDGEMENTS**

This work has been supported in part by NIH grants CA 085139 and CA 113004 and by the Harvard-MIT (HST) Athinoula A. Martinos Center for Biomedical Imaging and the Department of Radiology at Massachusetts General Hospital. We thank Dr. Chung-Kang Peng (Beth Israel Deaconess Medical Center, Harvard Medical School, Boston) for helpful discussions on the application of Detrended Fluctuation Analysis.

## **REFERENCES**

Alarcon, T., Byrne, H.M., & Maini, P.K., 2004. A mathematical model of the effects of hypoxia on the cell-cycle of normal and cancer cells. *J. theor. Biol.* 229, 395–411. doi:10.1016/j.jtbi.2004.04.016.

Araujo, R.P., Petricoin, E.F., & Liotta, L.A., 2005. A mathematical model of combination therapy using the EGFR signaling network. *Biosystems.* 80, 57-69.

Athale, C., Mansury, Y., & Deisboeck, T., 2005. Simulating the impact of a molecular 'decision-process' on cellular phenotype and multicellular patterns in brain tumors. *J. theor. Biol.* 233, 469-481. doi:10.1016/j.jtbi.2004.10.019.

Athale C.A., & Deisboeck T.S., 2006. The effects of EGF-receptor density on multiscale tumor growth patterns. *J. theor. Biol.* 238(4): 771-779. doi:10.1016/j.jtbi.2005.06.029.

Axelrod, R., Axelrod, D.E., & Pienta, K.J., 2006. Evolution of cooperation among tumor cells. *Proc. Natl. Acad. Sci. U.S.A.* 103(36), 13474-13479

Boussouar, F., & Benahmed, M., 1999. Epidermal growth factor regulates glucose metabolism through lactate dehydrogenase a messenger ribonucleic acid expression in cultured porcine sertoli cells. *Biol. Reprod.* 61, 1139-1145.

Buldyrev, S.V., Goldberger, A.L., Havlin, S., Peng, C.K., Stanley, H.E., Stanley, M.H.R., & Simons, M., 1993. Fractal landscapes and molecular evolution: modeling the myosin heavy chain gene family. *Biophys. J.* 65, 2673-2679.

Carmeliet, P., & Jain, R.K., 2000. Angiogenesis in cancer and other diseases. *Nature.* 407, 249-257.

Castro, M., Molina-Paris, C., & Deisboeck, T.S., 2005. Tumor growth instability and the onset of invasion. *Phys. Rev. E* 72, 041907. doi:10.1103/PhysRevE.72.041907

Chicoine, M.R., & Silbergeld, D.L., 1995. Assessment of brain tumor cell motility in vivo and in vitro. *J. Neurosurg.* 82, 615-622.

Chintala, S.K., Tonn, J.C., & Rao, J.S., 1999. Matrix metalloproteinases and their biological function in human gliomas. *Int. J. Devl Neuroscience*. 17, 495-502.

Choe, G., Park, J.K., Jouben-Steele, L., Kremen, T.J., Liao, L.M., Vinters, H.V., Cloughesy, T.F., & Mischel, P.S., 2002. Active matrix metalloproteinase 9 expression is associated with primary glioblastoma subtype. *Clin. Cancer Res*. 8, 2894-2901.

Christofori, G. 2006 New Signals from the invasive front. *Nature* 441(7092), 444-450.

Costa, L.D.F., Cintra, L.C., & Schubert, D., 2005. An integrated approach to characterization of cell movement. *Cytometry A*. 68(2), 92-100.

Deisboeck, T.S., Berents, M.E., Kansal, A.R., Torquato, S., Stepmmer-Rachamimov, A.O., & Chiocca, E.A., 2001, Pattern of self-organization in tumor systems: Complex growth dynamics in a novel brain tumor spheroid model. *Cell prolifer*. 34, 115-134.

Demuth, T., Reavie, L.B., Nakada, M., Nakada, N., Henrichs, E.A., Zhang, L., Wang Z.H., Deisboeck, T.S., & Berens, M.E., In preparation. A molecular 'switch' between cell migration and proliferation in human gliomas: Characterizing the role of Phospholipase  $C\gamma$  and its MKK3 signaling effector.

Dittmar, T., Husemann, A., Schewe, Y., Nofer, J.R., Niggemann, B., Zanker, K.S., & Brandt, B.H., 2002. Induction of cancer cell migration by epidermal growth factor is initiated by specific phosphorylation of tyrosine 1248 of c-erbB-2 receptor via EGFR. *Faseb J*. 16(13), 1823-1825.

Forsten, K., & Lauffenburger D., 1992. Autocrine ligand binding to cell receptors. *Biophys. J.* 61, 518-529.

Freyer, J.P., & Sutherland R.M., 1986. Regulation of growth saturation and development of necrosis in EMT6/Ro multicellular spheroids by the glucose and oxygen supply. *Cancer Res.* 46 (7), 3504-3512.

Giese, A., Loo, M.A., Tran, N., Haskett, D., Coons, S.W., & Berens, M.E., 1996. Dichotomy of astrocytoma migration and proliferation. *Int. J. Cancer* 67, 275-282.

Gordon, V.D., Valentine, M.T., Gardel, M.L., Andor-ardo, D., Dennison, S., Bogdanov, A.A., Weitz, D.A., & Deisboeck, T.S., 2003. Measuring the mechanical stress induced by an expanding multicellular tumor system: a case study. *Exp. Cell Res.* 289, 58-66.

Greenberg, M. S., 2001. *Handbook of Neurosurgery*. Greenberg Graphics, Lakeland, FL, USA.

Gruetter, R., Novotny, E.J., Boulware, S.D., Rothman, L.D., Mason, G.F., Shulman, G.I., Shulman R.G., & Tamborlane, W.V., 1992. Direct measurement of brain glucose concentration in human by  $^{13}\text{C}$  NMR spectroscopy. *Proc. Natl. Acad. Sci. U.S.A.* 89, 1109-1112.

Habib, S., Molina-Paris, C., & Deisboeck, T.S., 2003. Complex dynamics of tumors: modeling an emerging brain tumor system using a set of coupled reaction-diffusion equations. *Physica A.* 327, 501-524.

Hakim, S., 1971. Biomechanics of hydrocephalus. *Acta Neurol Latinoam* 1, Suppl. 1, 169-194.

Hanahan, D., & Weinberg R.A., 2000. The hallmarks of cancer. *Cell* 100(1), 57-70.

Hausdorff, J.M., Peng, C.K., Ladin, Z., Wei. J.Y., & Goldberger AL, 1995. Is walking a random walk? Evidence for long-range correlations in stride interval of human gait. *J. Appl. Physiol.* 78, 349-358.

Jain, R.K., 1987. Transport of molecules in the tumor interstitium: a review. *Cancer Res.* 47, 3039-3051.

Jones, G., Machade, J., & Merlo A., 2001. Loss of focal adhesion kinase (FAK) inhibits epidermal growth factor receptor-dependent migration and induces aggregation of NH<sub>2</sub>-Terminal FAK in the nuclei of apoptotic glioblastoma cells. *Cancer Res.* 62, 4978-4981.

Kaufman, L. J., Brangwynne, C. P., Kasza, K. E., Filippidi, E., Gordon, V. D., Deisboeck, T. S., & Weitz, D.A., 2005. Glioma Expansion in Collagen I Matrices: Analyzing collagen concentration-dependent growth and motility patterns. *Biophys. J.* 89, 635-650.

Khoshyomn, S., Penar, P.L., Rossi, J., Wells, A., Abramson, D.L., & Bhushan, A., 1999. Inhibition of phospholipase C-gamma1 activation blocks glioma cell motility and invasion of fetal rat brain aggregates. *Neurosurgery* 44(3), 568-577.

Kleihues, P., Soylemezoglu, F., Schauble, B., Scheithauer, B.W., & Burger, P.C., 1995. Histopathology, classification and grading of gliomas. *GLIA.* 15, 211-221.

Lund-Johansen, M., Bjerkvig, R., Humphrey, P.A., Bigner, S.H., Bigner, D.D., & Laerum, O.D., 1990. Effect of epidermal growth factor on glioma cell growth, migration, and invasion in vitro. *Cancer Res.* 50(18), 6039-6044.

Maley, C. C., Galipeau, P. C., Finley, J.C., Wongsurawat, V. J., Li, X., Sanchez, C.A., Paulson, T.G., Blount, P. L., Risques, R., Rabinovitch, P. S., & Reid, B. J., 2006. Genetic clonal diversity predicts progression to esophageal adenocarcinoma. *Nature Genetics.* 38(4), 468-473.

Mansury, Y., Kimura, M., Lobo, J., & Deisboeck, T., 2002. Emerging patterns in tumor systems: simulating the dynamics of multicellular clusters with an agent-based spatial agglomeration model. *J. theor. Biol.* 219, 343–370. doi:10.1006/jtbi.2002.3131.

Mansury, Y., & Deisboeck, T., 2003. The impact of “search precision” in an agent-based tumor model. *J. theor. Biol.* 224, 325–337. doi:10.1016/S0022-5193(03)00169-3.

Mansury, Y., & Deisboeck, T., 2004a. Simulating ‘structure-function’ patterns of malignant brain tumors. *Physica A* 331, 219–232. 10.1016/S0378-4371(03)00837-9.

Mansury, Y., & Deisboeck, T., 2004b. Simulating the time series of a selected gene expression profile in an agent-based tumor model. *Physica D* 196, 193–204. doi:10.1016/j.physd.2004.04.008.

Marmarou, A., Shulman, K., & Lamorgese, J., 1975. Compartmental analysis of compliance and outflow resistance of the cerebrospinal fluid system. *Neurosurg.* 43, 523-534.

Moskal, T., Huang, S., Ellis, L., Fritsche H., & Chakrabarty, S., 1995. Serum levels of transforming growth factor alpha in gastrointestinal cancer patients. *Cancer Epidemiol Biomarkers Prev.* 4, 127-131.

Nagashima, T., Tamaki, N., Matsumoto, S., Horwitz, B., & Seguchi, Y., 1987. Biomechanics of hydrocephalus: a new theoretical model. *Neurosurgery.* 21, 898-904.

Nakano, A., Tani, E., Miyazaki, K., Yamamoto, Y., & Furuyama, J., 1995. Matrix metalloproteinases and tissue inhibitors of metalloproteinases in human gliomas. *J. Neurosurg.* 83, 298-307.

Natarajan, M., Hecker, T.P., & Gladson, C.L., 2003. FAK Signaling in Anaplastic Astrocytoma and Glioblastoma Tumors. *Cancer J.* 9(2), 126-133.

Ohgaki, H., Schauble, B., zur Hausen, A., von Ammon, K., & Kleihues, P., 1995. The role of transformation-associated genes in the evolution of astrocytic brain tumors. *Virchows Arch.* 427, 113-118.

Ossadnik, S.M., Buldyrev, S.V., Goldberger, A.L., Havlin, S., Mantegna, R.N., Peng, C.K., Simons, M., & Stanley HE., 1994. Correlation approach to identify coding regions in DNA sequences. *Biophys. J.* 67, 64-70.

Pena, A., Bolton, M.D., Whitehouse, H., & Pickard, J.D., 1999. Effects of brain ventricular shape on periventricular biomechanics: a finite-element analysis. *Neurosurgery*. 45(1), 107-118.

Peng, C.K., Buldyrev, S.V., Havlin, S., Simons, M., Stanley, H.E., & Goldberger, A.L., 1994. On the mosaic organization of DNA nucleotides. *Phys. Rev. E*. 49, 1685-1688.

Peng, C.K., Havlin, S., & Goldberger, A.L., 1995. Quantification of scaling exponents and crossover phenomena in nonstationary heartbeat time series. *Chaos*. 5(1), 82-87.

Riemenschneider, M.J., Mueller, W., Betensky, R.A., Mohapatra, G., & Louis D.N., 2005. In situ analysis of integrin and growth factor receptor signaling pathways in human glioblastoma suggests overlapping relationships with focal adhesion kinase activation. *Am. J. Pathol.* 167, 1379-1387.

Runowicz, C., Cherry, S., & Lange, D., 2005. *The answer to cancer: stop it before it starts, arrest it in this earliest states, prevent it from coming back*. Rodale Books Press, New York, NY, USA.

Sander, L.M., & Deisboeck, T.S., 2002. Growth patterns of microscopic brain tumors. *Phys. Rev. E*. 66, 051901.

Schoeberl, B., Elichler-Jonsson, C., Gilles, E.D., & Muller, G., 2002. Computational modeling of the dynamics of the MAP kinase cascade activated by surface and internalized EGF receptors. *Nature biotechnology*, 20370-20375.

Shrivastava, V., Mishra, A. K., Dwarakanath, B. S., & Ravindranath, T., 2006. Enhancement of radionuclide induced cytotoxicity by 2-deoxy-D-glucose in human tumor cell lines. *JCRT*. 2(2), 57-64.

Sidransky, D., Mikkelsen, T., Schwechhelmer, K., Rosenblum, M.L., Cavanee, W., & Vogelstein, B., 1992. Clonal expansion of p53 mutant cells is associated with brain tumor progression. *Nature* 355, 846-847.

Sklar, F.H., & Elashvili, I., 1977. The pressure-volume function of brain elasticity. *J. Neurosurg.* 47, 670-679.

Smith, H.G., 2004. Reversing cancer: a journey from cancer to cure. International center for nutritional research, Inc, Langhorne, PA, USA.

Sole, R.V., & Deisboeck, T.S., 2004. An error catastrophe in cancer. *J. theor. Biol.* 228, 47-54. doi:10.1016/j.jtbi.2003.08.018.

Steinbach, J.P., Klumpp, A., Wolburg, H., & Weller M., 2004. Inhibition of epidermal growth factor receptor signaling protects human malignant glioma cells from hypoxia-induced cell death. *Cancer Res.* 64, 1575-1578.

Swetina, J., & Schuster, P., 1982. Self-replication with errors. a model for polynucleotide replication. *Biophys. Chem.* 16, 329-345.

Thorne, R.G., Hrabetova S., & Nicholson, C., 2004. Diffuse of epidermal growth factor in rat brain extracellular space measured by integrative optical imaging. *J. Neurophysiol.* 92, 3471-3481.

Tyson, J.J., & Novak, B., 2001. Regulation of the eukaryotic cell-cycle: molecular antagonism, hysteresis, and irreversible transitions. *J. theor. Biol.* 210, 249–263. doi:10.1006/jtbi.2001.2293.

Ware, M.F., Wells, A., & Lauffenburger, D., 1998. Epidermal growth factor alters fibroblast migration speed and directional persistence reciprocally and in a matrix-dependent manner. *J. Cell Sci.* 111, 2423-2432.

Westermarck, B., Magnusson, A., & Heldin, C., 1982. Effect of epidermal growth factor on membrane motility and cell locomotion in cultures of human clonal gliomas cells. *J. Neurosci. Res.* 8, 491-507.

Wolfram, S., 1994. *Cellular Automata and Complexity: Collected Papers*. Addison-Wesley, Reading, MA, USA.

Zhang, L., Athale, C.A., & Deisboeck, T.S., 2007. Development of a three-dimensional multiscale agent-based tumor model: Simulating gene-protein interaction profiles, cell phenotypes & multicellular patterns in brain cancer. *J. Theor. Biol.* 244(1), 96-107. doi:10.1016/j.jtbi.2006.06.034.

## CAPTIONS

**Figure 1.** Shown is the underlying 3D lattice, with Cube 4 harboring the nutrient source.

**Figure 2.** The diagram displays the mutational steps that constitute the genetic progression pathway from clone A to E.

**Figure 3.** The EGFR gene-protein interaction network (see text for details).

**Figure 4.** Depicted is the tumor system volume ( $y$ -axis) over time ( $x$ -axis). Shown are mean values of 10 simulation runs with random standard deviation (*grey*) of the glucose concentration at a range between 50 and 60 nmol/lattice site.

**Figure 5. (a)** The schematic shows the separation of the tumor into three regions (*dotted lines*) with varying distance to the nutrient source (*black circle* in Cube 4; compare with **Fig. 1**). **(b)** Depicted is the Shannon Index ( $y$ -axis) over time ( $x$ -axis) for these three distinct regions. Shown is the result of 10 runs with standard deviation.

**Figure 6.** Shown are 3D snapshots of the tumor system at time step  $t = 110$  **(a)**,  $t = 225$  **(b)**,  $t = 310$  **(c)**. The *red circle* depicts the location of the nutrient source (compare with **Fig. 1**). Note, the light and dark *green* colors represent cells of clone A in their proliferation state and migration state, respectively; light and dark *blue* represent cells of clone B in proliferation and migration states; light and dark *yellow* represent cells of clone C in proliferation and migration state; light and dark *purple* represent cells of clone D in proliferation and migration states; light and dark *red* represent cells of clone E in proliferation and migration states. Finally, light and dark *grey* represent cells in the quiescence and apoptosis states, respectively, for clones A-E.

**Figure 7.** Shown is the expansion rate (*y-axis*) of regions 1, 2 and 3 over time (*x-axis*).

**Figure 8.** Displayed is the expansion rate (*y-axis*) of clone A, B, C, D and E over time (*x-axis*).

**Figure 9.** Depicted is the phenotypic spectrum (*y-axis*) for clone (a) A, (b) B, (c) C, (d) D and (e) E over time (*x-axis*).

**Figure 10.** Displays the DFA analysis for the various clones, with  $\lg F(n)$  (*y-axis*) and  $\lg n$  (*x-axis*).

**Figure 11.** Depicted is the displacement effectiveness (*y-axis*) for the five distinct clones (*x-axis*).

**Figure 12.** Shown is the relationship between the percentage change of the clonal expansion rate (*z-axis*), EGFR density (*y-axis*) and active  $PLC_\gamma$  (*x-axis*) for clone (a) A, (b) B, (c) C, (d) D and (e) E.

**Table 1.** Details cell cycle times and proliferation periods for clone A to E.

**Table 2.** Coefficients of the tumor heterogeneity model taken from the literature (Athale et al., 2004; Thorne et al., 2004; Sander et al., 2002, Pena, et al., 1999, Sklar & Elashvili, 1977, Gruetter et al., 1992, Zhang et al., 2007).

**Table 3.** Lists chemotactic search precision, as well as the degrees of spatial search behavior for clone A to E.

**FIGURES & TABLES**

**FIGURE 1.**

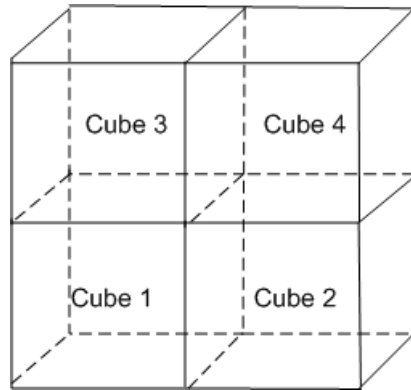


**FIGURE 2.**

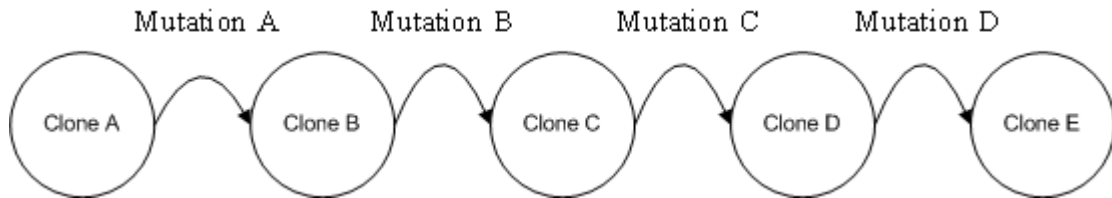


**FIGURE 3.**

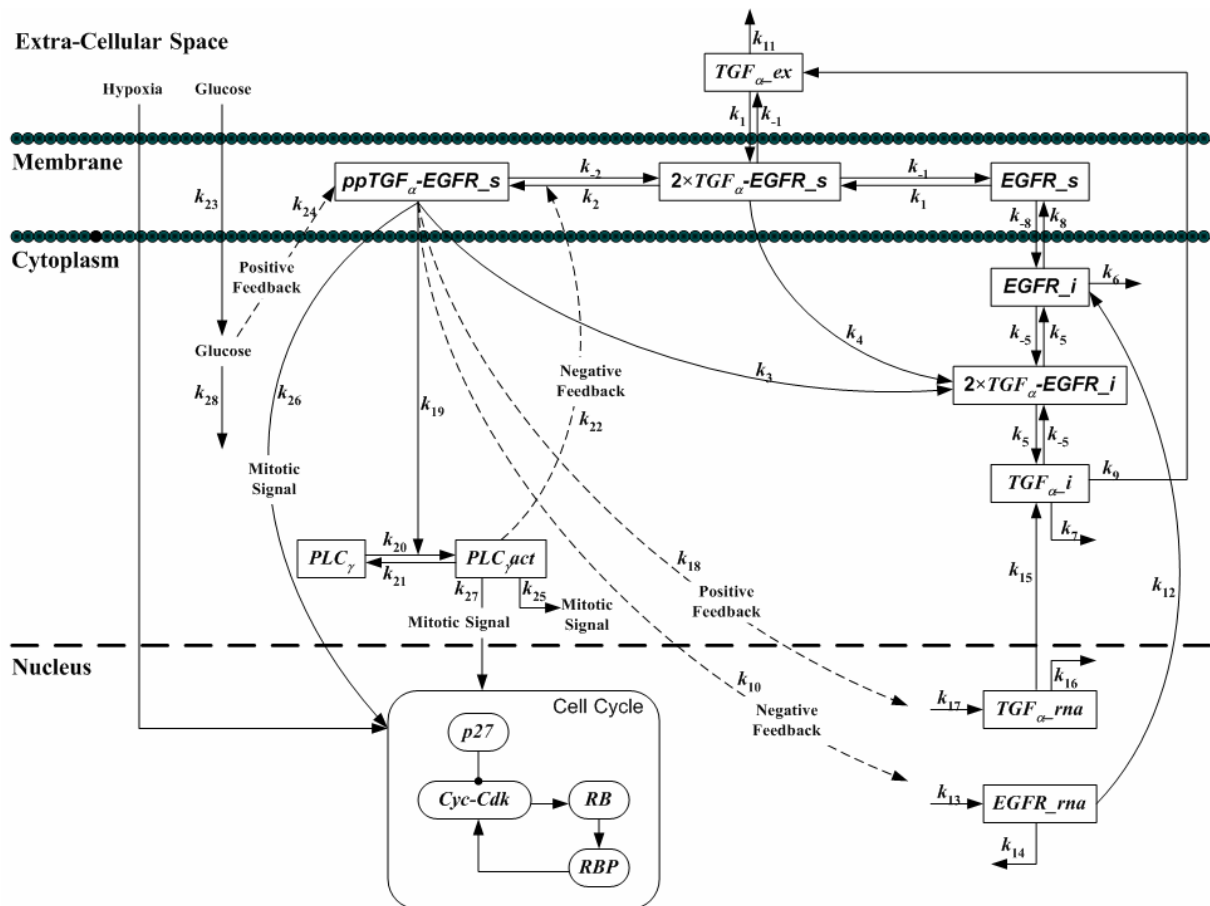


**FIGURE 4.**

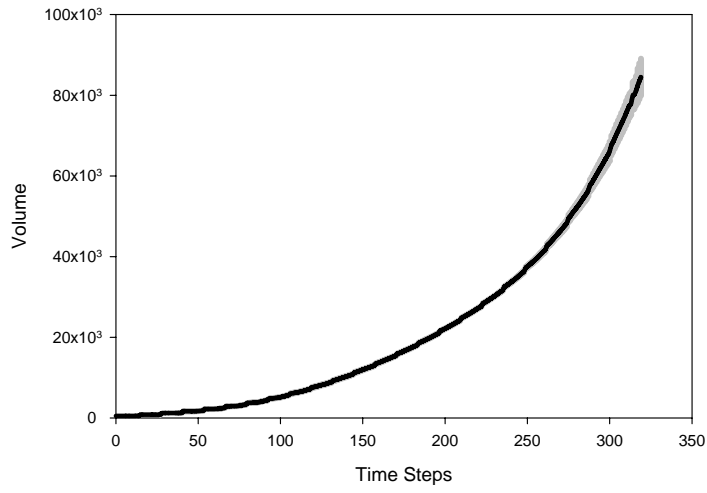


**FIGURE 5. (a)**

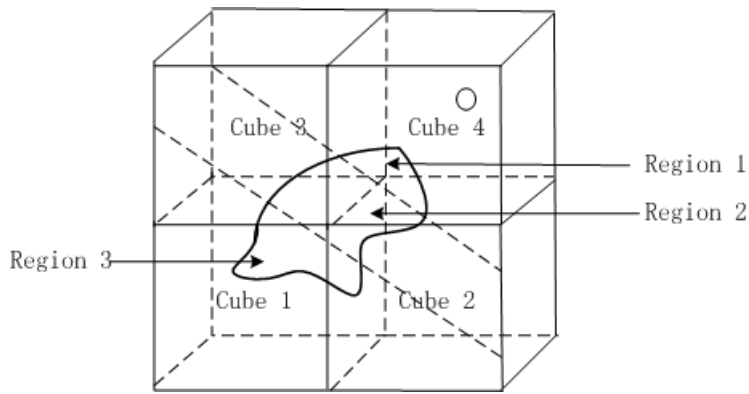


**FIGURE 5. (b)**

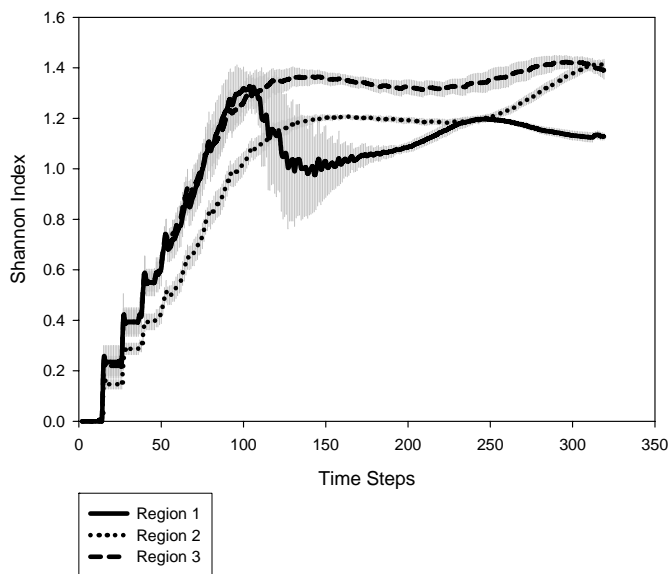


**FIGURE 6. (a)**

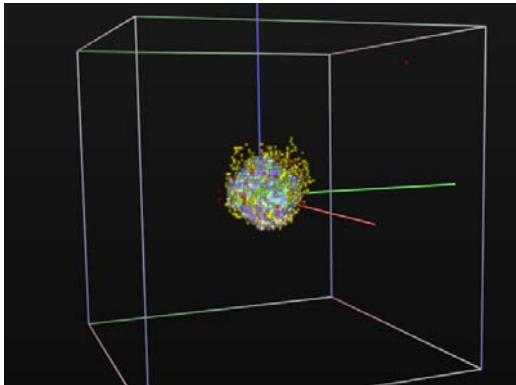


**FIGURE 6. (b)**

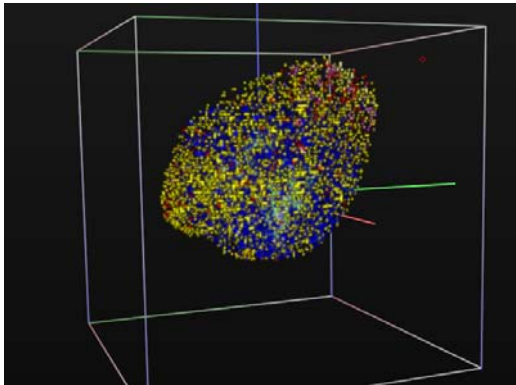


**FIGURE 6. (c)**

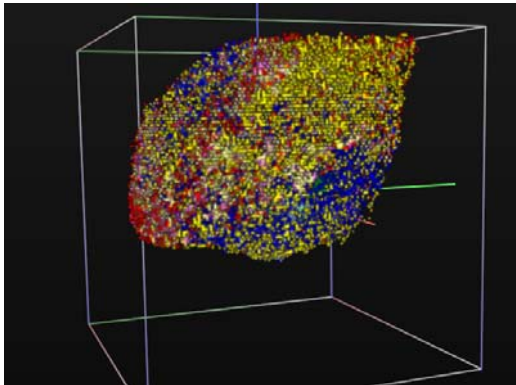


**FIGURE 7.**

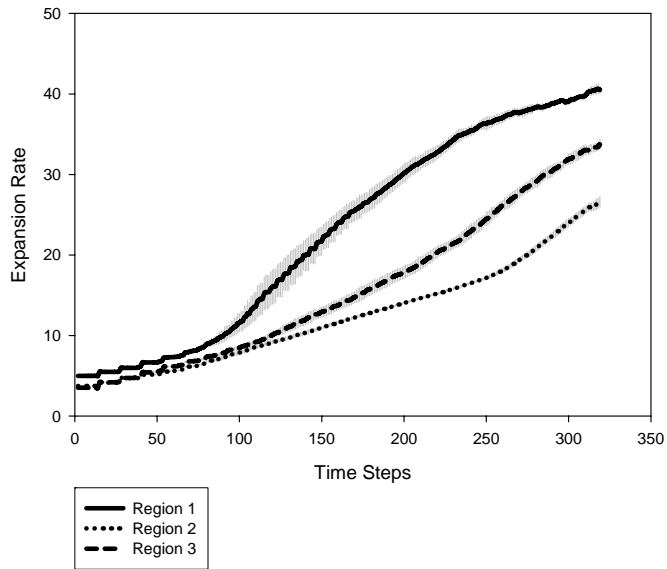


**FIGURE 8.**

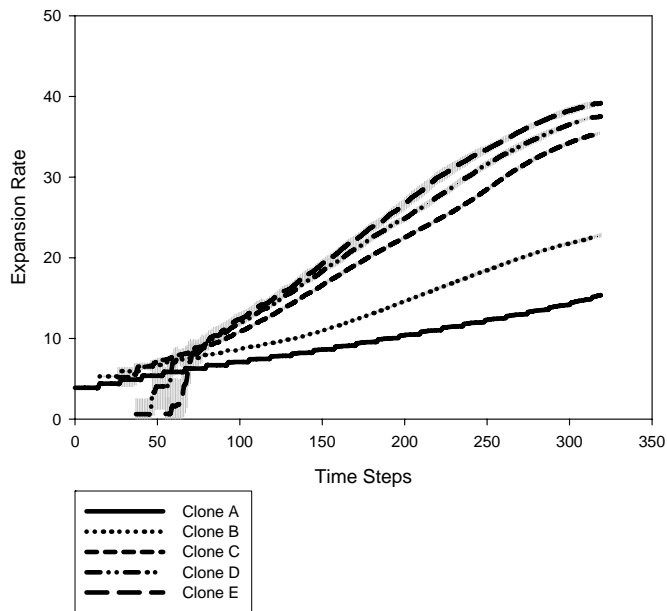


**FIGURE 9. (a)**

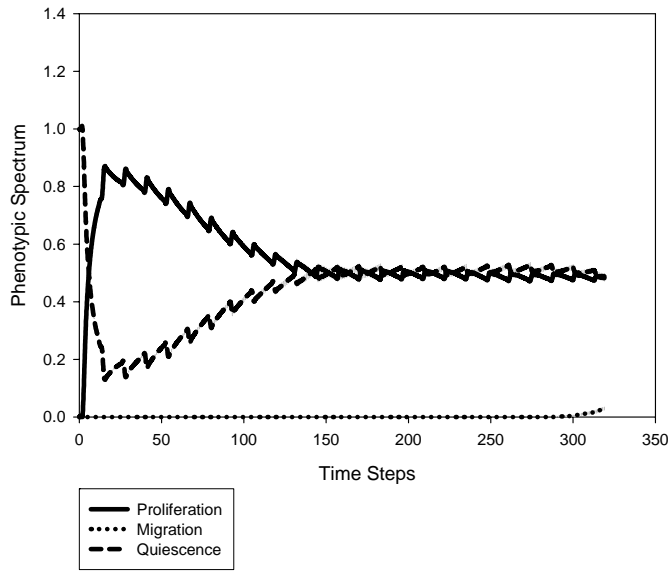


**FIGURE 9. (b)**

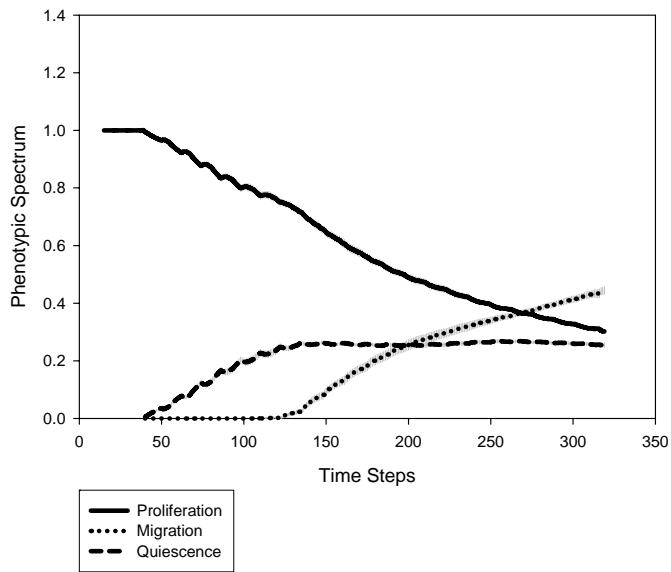


**FIGURE 9. (c)**

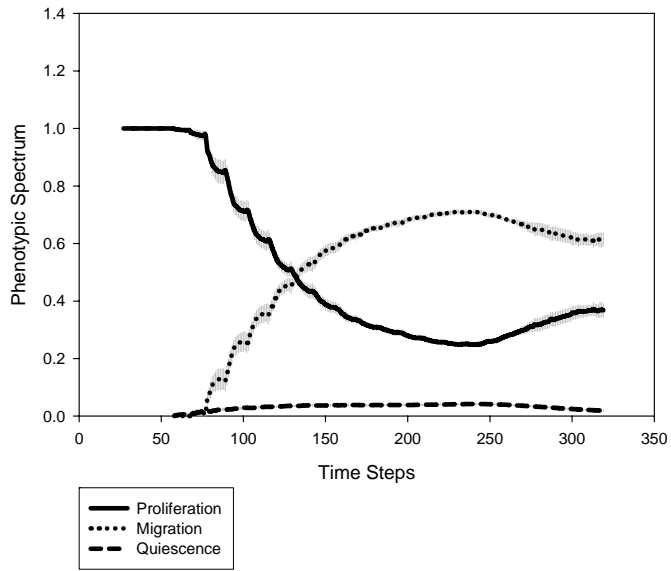


**FIGURE 9. (d)**

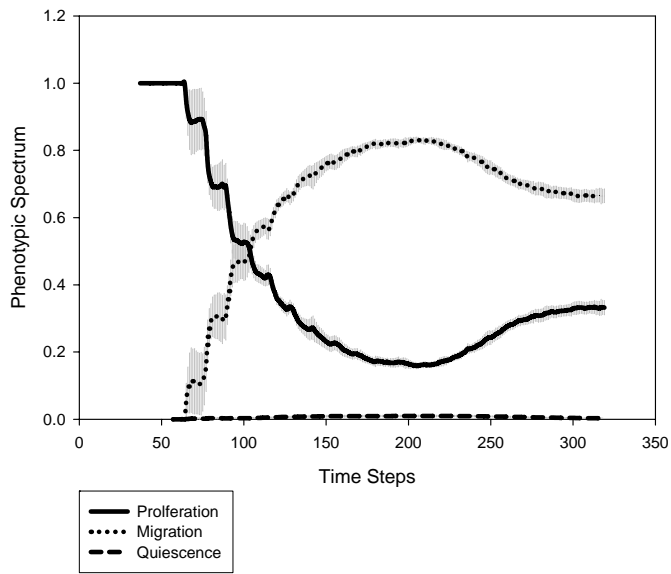


**FIGURE 9. (e)**

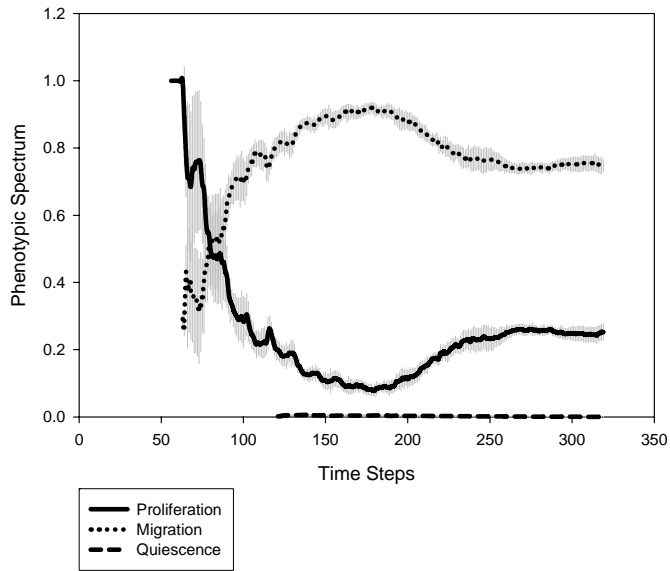


**FIGURE 10.**

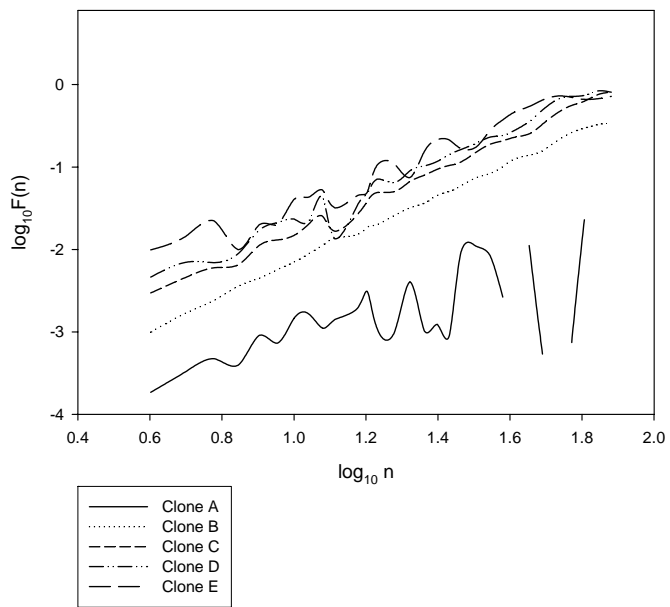


**FIGURE 11.**

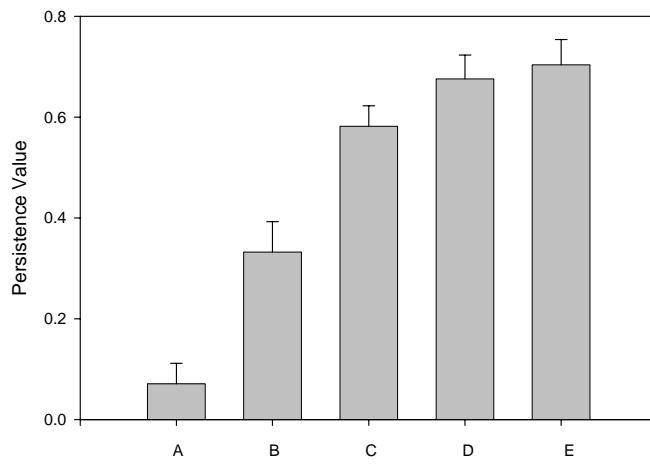


**FIGURE 12. (a)**

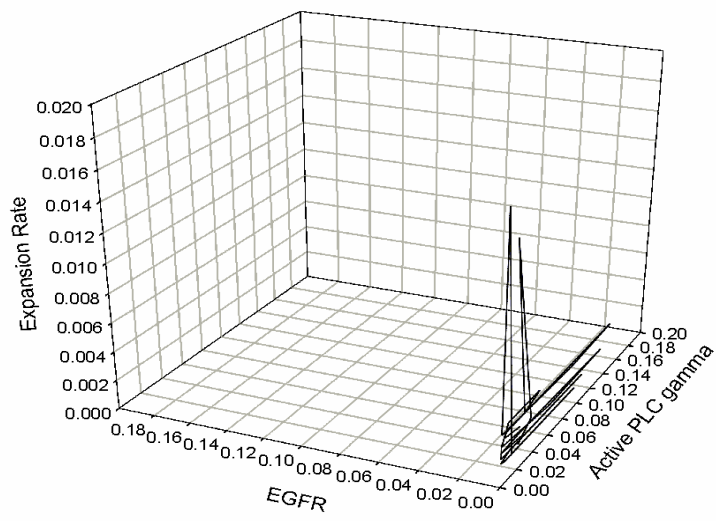


**FIGURE 12. (b)**

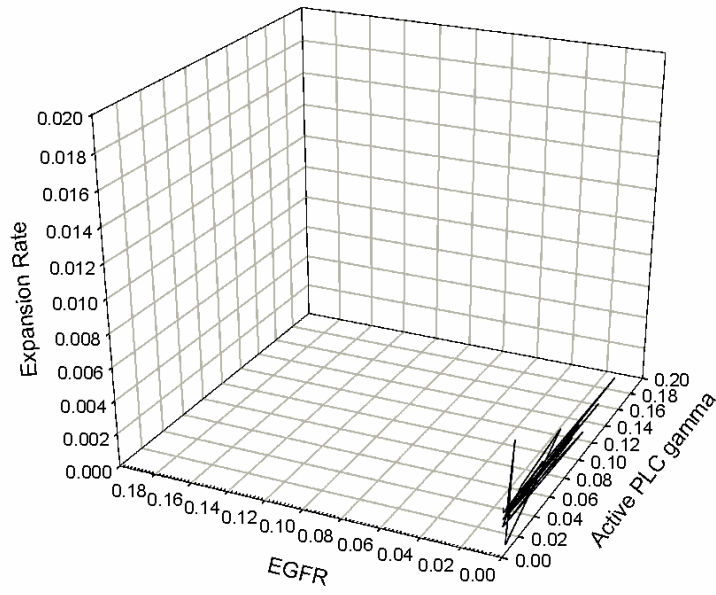


**FIGURE 12. (c)**

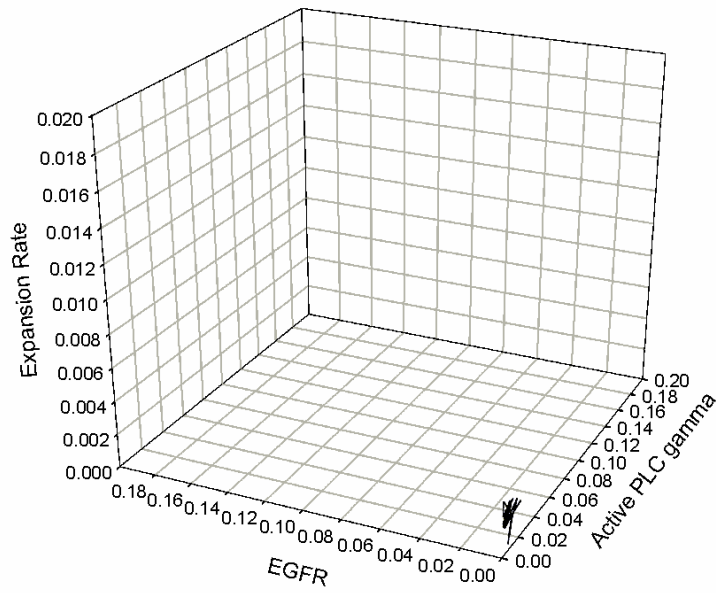


**FIGURE 12. (d)**

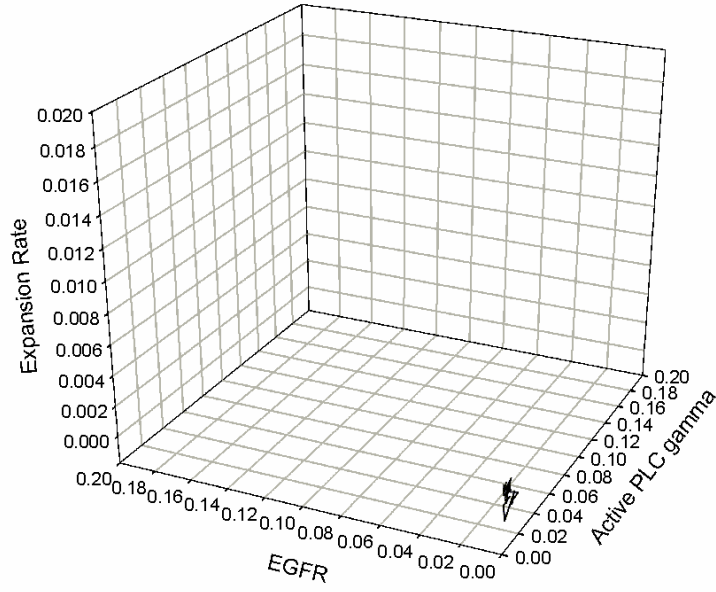


**FIGURE 12. (e)**

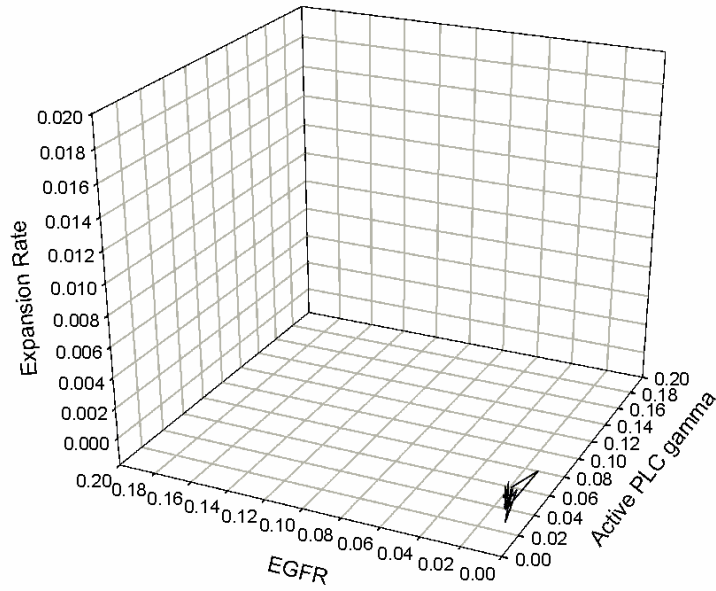


**TABLE 1.**

Clone type	Cell cycle	Proliferation period
A	T	4T
B	T	3.5T
C	T	3T
D	T	2.5T
E	T	2T

**TABLE 2.**

$r_A$	$3.85 \times 10^{-12}$	<i>mol/step</i>	Glucose uptake coefficient for clone A
$r_B$	$4 \times 10^{-12}$	<i>mol/step</i>	Glucose uptake coefficient for clone B
$r_C$	$7.7 \times 10^{-12}$	<i>mol/step</i>	Glucose uptake coefficient for clone C
$r_D$	$1.54 \times 10^{-11}$	<i>mol/step</i>	Glucose uptake coefficient for clone D
$r_E$	$3.08 \times 10^{-11}$	<i>mol/step</i>	Glucose uptake coefficient for clone E
$K$	$1.6 \times 10^{-11}$	$m^4 N^{-1} s^{-1}$	Hydraulic permeability
$D_1$	$6.7 \times 10^{-7}$	$cm^2 s^{-1}$	Diffusion coefficient of glucose
$D_2$	$5.18 \times 10^{-7}$	$cm^2 s^{-1}$	Diffusion coefficient of $TGF_\alpha$
$D_o$	$8 \times 10^{-5}$	$cm^2 s^{-1}$	Diffusion coefficient of oxygen tension
$T_m$	$147 \pm 18$	<i>pg / ml</i>	Maximum concentration of $TGF_\alpha$
$G_a$	$0.72 \times 10^{-9}$	<i>mol/site</i>	Normal concentration of glucose
$G_m$	$2.36 \times 10^{-9}$	<i>mol/site</i>	Maximum concentration of glucose
$S_T$	0.3	<i>molecules/min</i>	Secretion rate of $TGF_\alpha$
$k_a$	0.0017	<i>Dimensionless Constant (DC)</i>	Normal concentration of oxygen
$k_m$	0.0025	<i>DC</i>	Maximum concentration of oxygen
$\eta$	1.8	<i>DC</i>	Significant reduction weight
$\omega$	10	<i>Hg <math>\mu m/step</math></i>	Weight constant for migration speed
$\gamma_1$	$0.33 \times 10^{-4}$	<i>DC</i>	Scale to adjust the difference between $TGF_\alpha$ and mechanical resistance
$\gamma_2$	$0.33 \times 10^{-4}$	<i>DC</i>	Scale to adjust the difference between glucose and mechanical resistance

**TABLE 3.**

Clone type	Search precision	Proliferation	Migration
A	0.5	Von Neumann	Von Neumann
B	0.6	Von Neumann	Moore
C	0.7	Moore	Moore
D	0.7	Moore	Moore
E	0.7	Moore	Moore